Chinese Chemical Letters 32 (2021) 2453–2458

Contents lists available at ScienceDirect

Chinese Chemical Letters

journal homepage: www.elsevier.com/locate/cclet

Communication

Hollow polyhedron structure of amorphous Ni-Co-S/$Co(OH)_2$ for high performance supercapacitors

Xixi Zhang, Guangmeng Qu, Zonghua Wang, Guotao Xiang, Shuhua Hao, Xiaoke Wang, Xijin Xu*, Wenxuan Ma, Gang Zhao*

School of Physics and Technology, University of Jinan, Ji'nan 250022, China

ARTICLE INFO

Article history:
Received 19 December 2020
Received in revised form 17 January 2021
Accepted 19 January 2021
Available online 27 January 2021

Keywords:
Ion exchange
Amorphous
β-$Co(OH)_2$
Hollow polyhedron
Supercapacitor

ABSTRACT

In power storage technology, ion exchange is widely used to modify the electronic structures of electrode materials to stimulate their electrochemical properties. Here, we proposed a multistep ion exchange (cation exchange and anion exchange) strategy to synthesize amorphous Ni-Co-S and β-$Co(OH)_2$ hybrid nanomaterials with a hollow polyhedron structures. The synergistic effects of different components and the remarkable superiorities of hollow structure endow Ni-Co-S/$Co(OH)_2$ electrode with outstanding electrochemical performance, including ultra-high specific capacity (1440.0 C/g at 1 A/g), superior capacitance retention rate (79.1% retention at 20 A/g) and long operating lifespan (81.4% retention after 5000 cycles). Moreover, the corresponding hybrid supercapacitor enjoys a high energy density of 58.4 Wh/kg at the power density of 0.8 kW/kg, and a decent cyclability that the capacitances are maintained at 80.8% compared with the initial capacitance. This research presents a high-performance electrode material and provides a promising route for the construction of electrode materials for supercapacitors with both structural and component advantages.

In contemporary world energy consumption rose sharply, energy production and consumption has affected the global climate change, causing environmental pollution, ecological destruction and a series of energy security. Therefore, taking effective measures to develop clean and sustainable energy storage and conversion technology is imperative, such as supercapacitors, ion-batteries [1–5]. As a burgeoning energy storage device between traditional electrolytic capacitors and batteries, supercapacitors with the virtues of high power density, ultrafast charging/discharging, long life and operating safety, have been widely applied in electronic and hybrid power equipment [6–9]. However, compared with conventional rechargeable batteries, the crucial issue of lower energy density still limiting the application of supercapacitors. Hence, how to improve the energy density of supercapacitors without sacrificing inherent strengths has become the focus of researchhotspot [10,11].

Electrode material is the most crucial factor that affects the performance of supercapacitors. In long-term studies, miscellaneous materials have been explored as the cathodes of asymmetric supercapacitors [12–14]. Especially, transition metal oxide/hydroxide with inexpensive cost and abundant reserves have triggered intense attentions from researchers, due to their reversible dynamical reactions on the surface materials rooting from rich redox valence states. Among them, nickel-cobalt based oxide (*e.g.*, Co_3O_4, NiO) is considered as one of the most valuable electrode materials for supercapacitors on account of their intrinsic superiorities of high theoretical specific capacitance and non-toxicity [15–17]. However, owing to their poor conductivity and lower actual capacitance, the development and practical application of nickel-cobalt based oxide have been hindered to a large extent [18,19]. Compare with corresponding oxides, transition metal sulfides can deliver more trustworthy electrochemical activity higher conductivity, since metal sulfides possesses superior electronic structures and the electronegativity (2.5) of S element is weaker than O element. Moreover, rich valence and synergistic effect from different metal ions in polymetallic sulfide structure can provide abundant redox reactions, resulting in better electrochemical performance for electrode materials. Therefore, polymetallic transition metal sulfides with compelling electrochemical performance have become powerful candidates to complement or even replace oxide/hydroxide electrode materials [20,21]. Nonetheless, owing to the highly dependent on surface-active redox reaction, the charge storage process of available transition metal sulfide electrode materials tends to undergo a

* Corresponding authors.
E-mail addresses: sps_xuxj@ujn.edu.cn (X. Xu), sps_zhaog@ujn.edu.cn (G. Zhao).

https://doi.org/10.1016/j.cclet.2021.01.042

decreased reaction kinetics in higher rates, which result in unsatisfactory rate performance and charging-discharging stability [22]. Designing and synthesizing amorphous bimetallic sulfide electrode materials have identified as a promising avenue to solve the forementioned problems [23–27]. The reasons are that the amorphous phase materials hold a large random orientation bond with unsaturated electron configuration, which is beneficial to the adsorption of electrolyte ions [22]. Furthermore, the amorphous phase materials possess higher chemical reactivity, because flexibility of local structure in the amorphous phase can accelerate the charge transfer between the active site and the intermediate [25]. For example, Liu *et al.*, by using hydrothermal method, synthesized an amorphous Ni_xS_y@CoS electrode that could deliver the capacitance of 1750 F/g and retained 71.6% after 2000 cycles [26]. From the perspective of thermodynamics, the amorphous state is a metastable state of energy, and has inherent conditions for self-discharging heat and crystallization, so that the stability of amorphous materials during continuous charging and discharging operations is unreliable [23,24]. Consequently, it is conceivable that constructing a nanomaterial which simultaneously combines crystalline and amorphous structures will be a promising approach for supercapacitor electrodes.

Additionally, it is also necessary to design a reasonable structure to elevate the electrochemical performances of electrode materials. Bimetallic sulfides can be facilely reconstructed from their metal oxide/hydroxide precursors through ion exchange and the Kirkendall effect, and eventually establish a variety of forms such as nanosheets, nanowires, and hollow nanostructures [6,28–30]. Thereinto, hollow nanostructures can provide plentiful electrochemical active site, kinetically advantageous open structure and larger contact area between the electrolyte and the materials surface, assisting to elevate the specific capacitance of the electrode material. Moreover, the internal cavities can effectively prevent the volume expansion in the reaction process to promote the cyclic properties of the materials [31–33]. MOFs, featuring with porosity, high specific surface area and shape controllability, have been extensively used as a promising self-sacrificial template to construct hollow nanostructures in the fields of energy storage and conversion [34,35]. For instance, Wang *et al.* synthesized amorphous $CoNi_2S_4$ by reflux method [32], the electrode retained 71.6% compared to initial capacitance (1755 F/g) after 5000 cycles. Yu *et al.* synthesized polycrystalline $NiCo_2S_4$ [33], which could deliver the capacitance of 1382 F/g at 1 A/g and retain 70% after 10000 cycles. Therefore, it is necessary to design a reasonable electrode structure to give full play to the advantages of hollow structure and polycrystalline amorphous hybrid composition. Encouraged by above considerations, it can be predicted that the electrochemical performance of electrode materials can be significantly improved *via* constructing an amorphous and crystallized mixed material with hollow structure derived from MOFs template by a viably reasonable method.

Based on the conceptions, a multistep hydrothermal ion-exchange method was proposed to synthesize amorphous Ni-Co-S and polycrystalline $Co(OH)_2$ hybrid hollow polyhedral nanostructures by coordinating the electrochemical activity and stability of amorphous and crystalline phases in this paper. The resultant Ni-Co-S/$Co(OH)_2$ nanomaterial fully integrates the structural advantages of hollow polyhedrons and the component advantages of crystalline and amorphous structures synergistic effect, showing outstanding electrochemical performances. Furthermore, the corresponding hybrid supercapacitor, composed of capacitor-type active carbon (AC) as the negative electrode and battery-type Ni-Co-S/$Co(OH)_2$ as the positive electrode, exhibits ultrahigh energy density of 58.4 Wh/kg at the power density of 0.8 kW/kg and prominent cycling stability (maintained 80.8% of initial capacity after 5000 cycles).

Fig. S1 (Supporting information) shows the schematic synthesis process of Ni-Co-S/$Co(OH)_2$ with multistep ion substitution. Firstly, the regular dodecahedron ZIF-67 is fabricated by coordination bond reactions of $Co(NO_3)_2{\cdot}6H_2O$ and organic ligands (2-dimethylimidazole, $C_4H_6N_2$) in methanol solvent [34,35]. Then, the cation exchange (Ni^{2+} and Co^{2+}) process is implemented to prepare the Ni-Co LDH. During the step, the protons yielded by the hydrolysis of Ni^{2+} etched the Co-ZIF polyhedron organic framework, resulting in the releases of Co^{2+}. Since the solubility constant (K_{sp}) of $Co(OH)_2$ (2.5×10^{-16}) is very close to $Ni(OH)_2$ (2.8×10^{-16}) at 25 °C, the released Co^{2+} and Ni^{2+} from the solution hydrolyzes almost simultaneously to form hydroxides and deposit on the

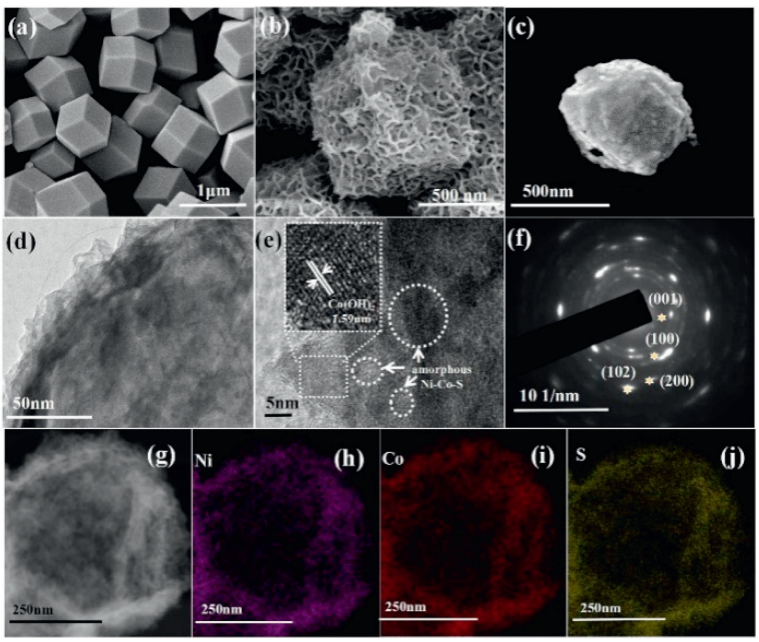

Fig. 1. SEM images: (a) ZIF-67; (b) Ni-Co LDH; (c) Ni-Co-S/$Co(OH)_2$. (d) TEM image of Ni-Co-S/$Co(OH)_2$. (e) HRTEM of Ni-Co-S/$Co(OH_)_2$. (f) SAED image of Ni-Co-S/$Co(OH)_2$. (g) EDS of Ni-Co-S/$Co(OH)_2$: (h) Ni, (i) Co, (j) S.

surface of the ZIF-67 polyhedron to organize a shell, the NiCo-LDH yolk-shell structure is formed [26,34–36].

Subsequently, $Na_2S{\cdot}9H_2O$ is employed as S^{2-} source and etcher-like agent to accomplish anion (OH^-) substitution and further etching. Under the hydrothermal condition, S^{2-} and metal-ions diffuse in and out at different rates, respectively. To compensate for the uneven mobility of materials, the high diffusivity of metal ions from inside to outside will lead to the formation of internal hollow structure [37,38]. While S^{2-} reacts with the shell NiCo-LDH to form Ni-Co-S, the internal Co^{2+} continues to diffuse outward due to the Kirkendall effect [6,33]. After the sulfuration reaction is completed, the hydrothermal process continues resulted in the internal Co^{2+} diffuses into the shell to form $Co(OH)_2$.

The SEM (Fig. 1a) and TEM image (Fig. S2a in Supporting information) show that synthesized ZIF-67 template featuring with smooth surface and uniform size displays morphological characteristics of regular rhombic dodecahedron about 500 nm in diameter, which is consistent with the previous reports [39]. The SEM and TEM images of the samples obtained after the cation exchange are illustrated in Fig. 1b and Fig. S2b (Supporting information). Obviously, the Ni-Co LDH well inherits the regular polyhedral features of the ZIF-67 template, and the yolk-shell structure is constructed by the preliminary proton etching, in which the surface of the shell is decorated by uniformly and vertically anchored Ni-Co LDH nanosheets. The SEM images of comparison samples (Ni-Co-O) are shown in Figs. S3a and b (Supporting information), exhibiting the core-shell structure. After reacted with $Na_2S{\cdot}9H_2O$ by hydrothermal, Ni-Co-S/$Co(OH)_2$ is fabricated. According to SEM image (Fig. 1c), it is obvious that the anion exchange and further etching do not change the polyhedral shape and rough surface. The TEM images in Fig. 1d and Fig. S2c (Supporting information) show Ni-Co-S/$Co(OH)_2$ with completely hollow cavities and functional shells consisting of abundant nanosheets. The hollow structure shortens the distance of ion diffusion path and retards volume expands while reacting to prevent the structure from being damaged and guaranteed long life. Besides, the external abundant ultrathin nanosheets can enlarge specific surface area and provide a mass of active sites for redox reaction. In the HRTEM image of Ni-Co-S/$Co(OH)_2$ (Fig. 1e), it can be observed that apparent lattice structure on the outside and blank disordered lattice part in the inner, indicating the $Co(OH)_2$ nanosheets with polycrystalline structure are distributed outside of the shell of hollow polyhedral, while the amorphous Ni-Co-S are distributed inside the shell. The spacing of the lattice is 1.59 nm, corresponding to (110) plane of β-$Co(OH)_2$ [40]. The selected electron diffraction (SAED) pattern (Fig. 1f) are assigned to (001), (100), (102) and (200) planes, which also reveals the polycrystalline structure of β-$Co(OH)_2$. Elemental distribution of the Ni-Co-S/$Co(OH)_2$ are investigated by EDS mapping (Figs. 1g–j and Fig. S4 in Supporting information), among which the C element originate from adsorption to the air. The elements of Ni, Co and S are distributed on the shell of the material, indicating the successful synthesis of hollow structure. Meanwhile, the small amount of N element means that the ligands in the ZIF-67 template were almost completely removed.

The crystalline structure and phase composition of the samples (ZIF-67, Ni-Co LDH and Ni-Co-S/$Co(OH)_2$) are determined by X-ray diffraction (XRD), which is presented in Fig. S5 (Supporting information). It can be observed that the prepared ZIF-67 and Ni-Co LDH match well with the crystal structures reported in the previous papers [41,42]. All diffraction peaks of Ni-Co-S/$Co(OH)_2$ can be assigned to the standard $Co(OH)_2$ (PDF card No. 30-0443). The peaks at 19.1°, 32.5°, 37.9°, 38.7°, 51.4°, 57.9° are matched with planes of (001), (100), (101), (002), (102), (110) faultlessly [43]. No diffraction peaks corresponding to Ni-Co-S compounds are observed in the XRD pattern, confirming its amorphous feature. The XRD image of contrast sample illustrated in Fig. S6 (Supporting information), it shows the mixed crystal of $NiCo_2O_4$ (PDF card No. 20-0781) and NiO (PDF card No. 44-1159), denoted as Ni-Co-O.

XPS characterization is performed to analyze the chemical composition and valence state of the material. From the survey spectrum in Fig. 2a, it can be found that Ni-Co-S/$Co(OH)_2$ consist of Co, Ni, S, O and C without other impurities. There are four main peaks existing in the interval of 856.2–880.9 eV in Ni 2p spectrum (Fig. 2b), including Ni $2p_{3/2}$, Ni $2p_{1/2}$ and two satellite peaks (indicated as "sat"). The two strong peaks located at 855.2 and 857.1 eV are ascribed to Ni^{2+} and Ni^{3+}, respectively [44]. In the period of binding energy from 770.5 eV to 812.3 eV of Co 2p (Fig. 2c), the four obvious peaks correspond to Co $2p_{3/2}$, Co $2p_{1/2}$ and two satellite peaks. Two peaks at 781.2 eV and 783.4 eV refer to Co^{3+} and Co^{2+}, in addition, 787.6 eV and 798.9 eV are Co^{3+} and Co^{2+}, severally [45]. Three peaks centered at 162.5 eV, 163.9 eV and 169.2 eV of S 2p in Fig. 2d correspond to S $2p_{3/2}$, S $2p_{1/2}$ and satellite peak [46].

Fig. S7 (Supporting information) shows nitrogen isothermal adsorption/desorption curve of the resultant sample, the isotherm can be classified as IV-type, which is a typical application of mesoporous materials. According to the Brunauer-Emmertt-Teller (BET) calculation method, the specific surface area of Ni-Co-S/$Co(OH)_2$ is calculated as 73.2 m^2/g. Besides, according to the shape of isothermal adsorption line and the analysis of hysteretic shape, the slit structure of the adsorption hole can be observed. Barrett-Joyner-Halenda (BJH) was used to calculate the average aperture is 2.3 nm. Generally, materials with large specific surface area and porosity are favorable for electron and ion diffusion [47].

To verify the application of Ni-Co-S/$Co(OH)_2$ electrode for supercapacitors, the electrochemical evaluates are implemented in a three electrode configuration. There is a pair of intense redox peaks in CV curves image (Fig. 3a) at the scan rates from 5 mV/s to 50 mV/s, exhibiting the occurrence of Co^{3+}/Co^{2+} and Ni^{3+}/Ni^{2+} redox reaction [48]. The corresponding redox reaction as follows:

$$2NiCoS + 2OH^- \leftrightarrow CoSOH + NiSOH + 2e^-$$

$$Co(OH)_2 + OH^- \leftrightarrow CoOOH + H_2O + e^-$$

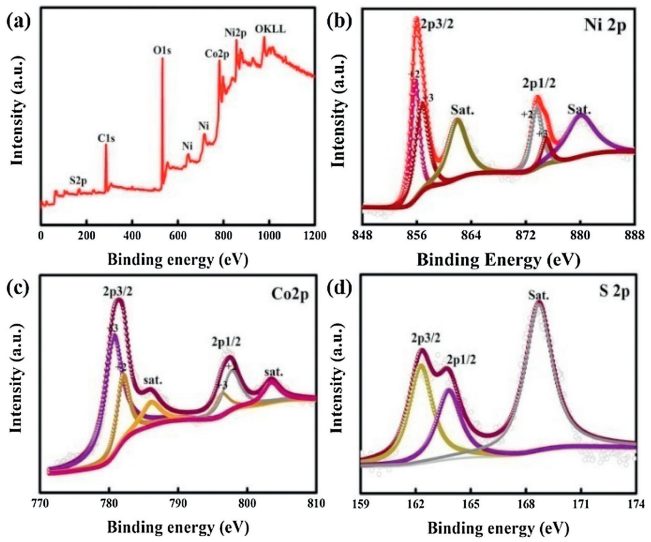

Fig. 2. (a) XPS spectra of Ni-Co-S/$Co(OH)_2$. (b-d) XPS spectra of Ni-Co-S/$Co(OH)_2$: (b) Ni spectrum; (c) Co spectrum; (d) S spectrum.

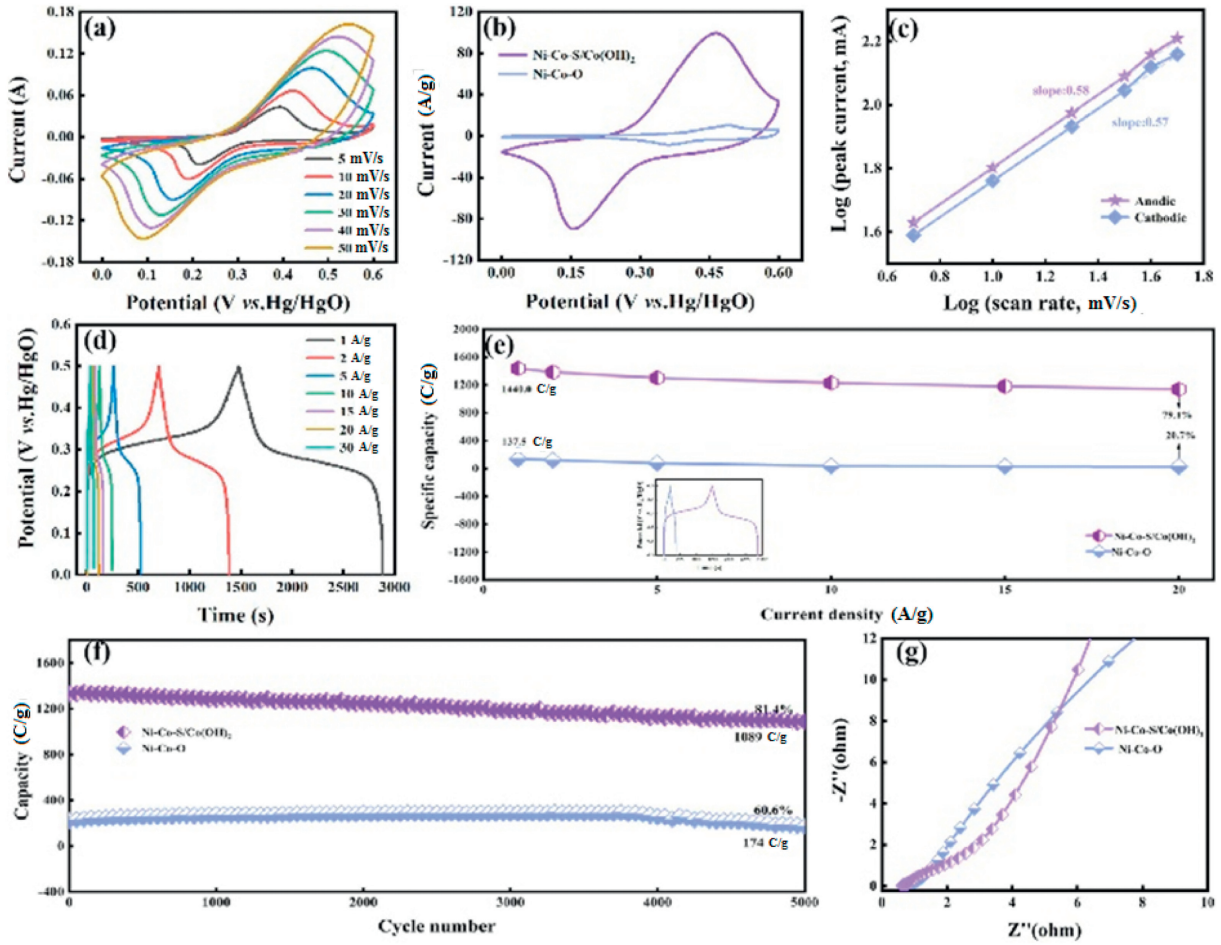

Fig. 3. (a) CV curves of Ni-Co-S/$Co(OH)_2$. (b) CV curves of Ni-Co-S/$Co(OH)_2$ and Ni-Co-O at 10 mV/s. (c) Logarithm relationship between anodic scan rates and peak current. (d) GCD curves of Ni-Co-S/$Co(OH)_2$ at different current densities from 1 A/g to 30 A/g. (e) Capacities rention of Ni-Co-S/$Co(OH)_2$ and Ni-Co-O, the illustration is a comparison of GCD of Co-S/$Co(OH)_2$ and Ni-Co-O at 1 A/g. (f) Cycling performance of Ni-Co-S/$Co(OH)_2$ at the current densities of 10 A/g. (g) EIS of Ni-Co-S/$Co(OH)_2$.

Amorphous Ni-Co-S and polycrystalline β-$Co(OH)_2$ simultaneously participate in redox reaction of the electrode, both contribute to electrode capacity.

Accompanied with the scan rates increased, redox peaks intensity enhanced, and the oxidation and reduction peaks moved to high and low potential respectively, which is due to the ions in the electrolyte are not enough to sufficiently stimulating the dense center inside the nano-architecture under high scan rates. And the *quasi*-symmetric profile of CV curves is well maintained, which indicates that battery electrode has ideal rate performance [49,50]. For comparison, Fig. S8 (Supporting information) are ascribed to the CV curves of Ni-Co-O. Particularly, there is a larger area of Ni-Co-S/$Co(OH)_2$ compared with contrast samples (Ni-Co-O) in Fig. 3b, confirming that it has better electrochemical properties which is due to the unique structure and component of Ni-Co-S/$Co(OH)_2$ electrodes. On the one side, hollow structure of the materials guarantees the abundant internal voids, ensuring full electrolyte penetration and a short electron ion diffusion path [18,51]. On the other side, the amorphous structure of Ni-Co-S can accelerate the transfer of charge and provide the larger surface area and more abundant redox active centers, which is conducive to be used as electrode materials with higher performance for electrochemical devices.

To explore the kinetics of Ni-Co-S/$Co(OH)_2$ electrode in redox reaction, the relation between current density and scanning rate is analyzed by formula S1 (Supporting information). The reaction kinetics is a characteristic by capacitive control process when *b* value is 1, while *b* of 0.5 indicates diffusion determined behavior. Fig. 3c represents the fitting lines and *b*-values at the scan rate from 5 mV/s to 50 mV/s, the slopes are 0.58 and 0.57 for anodic peaks and cathodic peaks. Which implies the charge storage process is mainly based ondiffusion process behavior [52] and the Ni-Co-S/Co$(OH)_2$ electrode possesses the fastest reaction kinetics.

The GCD curves of as-synthesized composite electrodes are demonstrated in Fig. 3d, the existence of voltage platform is consistent with the peak value of CV curves, confirming that there is a faradaic redox reaction. GCD curves shows almost symmetric shape, indicting highly reversible redox reactions.

Based on the formula S2 (Supporting information) of specific capacity under the three-electrode system, the specific capacity of Ni-Co-S/$Co(OH)_2$ electrode is 1440.0 C/g, 1385.3 C/g, 1303.2 C/g, 1230.6 C/g, 1181.3 C/g, 1139.1 C/g, respectively (at 1 A/g, 2 A/g, 5 A/g, 10 A/g, 15 A/g, 20 A/g). There is a retention of 79.1% even at high current density of 20 A/g, while Ni-Co-O is 20.7%. The values of specific capacity for Ni-Co-S/$Co(OH)_2$ electrode, observably higher than the Ni-Co-O electrode as shown in the illustration of Fig. 3e. After 5000 cycles (Fig. 3f), the capacitance retention rate is as high as 81.4%. It follows that the amorphous and polycrystalline hybrid structure not only improves the capacity of the electrode material, but also enhances its stability.

To gain more insight into the electrochemical behavior of supercapacitors based on different electrode materials, electrochemical impedance spectroscopy (EIS) measurements are performed, as shown in Fig. 3g. The measured impedance data are analyzed by fitting to an equivalent electrical circuit (Fig. S9 in

Supporting information), which is composed of equivalent series resistance (R_s), charge-transfer resistance (R_{ct}), constant-phase element (C_d) [53]. The R_s includes the intrinsic resistance of active materials, ionic resistance of electrolyte, and contact resistance at the active material/current collector interface. The diameter of the semicircle corresponding to R_{ct} displays the charge transfer process at the electrode-electrolyte interface. The impedance spectrum of the low-frequency region shows that Ni-Co-S/$Co(OH)_2$ has a large liner, which indicates the material has a lower diffusion limit. In the high-frequency region, Ni-Co-S has a smaller R_s and R_{ct}. The smaller R_{ct} shows the excellent dispersion of the material and the close combination of a large number of interstices with the base, resulting to the higher specific capacitance, indicating that the composite nanostructures electrode is a promising supercapacitor electrode [15,28]. The excellent electrochemical performance is mainly attributed to its unique hollow structure and the mixed structure of amorphous and polycrystalline: (1) The hollow structure with large specific surface area can increase the contact area between active materials and electrolytes. Besides, the internal voids ensure the full diffusion coefficient of electrolyte penetration. (2) The hollow structure provides buffer space to moderate the volume change in the charge storage process. (3) The hybrid structure not only achieves the flexibility of internal structure of amorphous phase to accelerate the charge transfer between active site and intermediate, but also realizes the stability of crystal structure [31,32,54].

In order to further investigate the practical properties of Ni-Co-S/$Co(OH)_2$, electrochemical performances measurements of corresponding asymmetric supercapacitors were carried out. Fig. 4a shows schematic illustration of the Ni-Co-S/$Co(OH)_2$//AC hybrid supercapacitor assembled with Ni-Co-S/$Co(OH)_2$ as the positive electrode and AC as the negative electrode, PVA-KOH gel as the electrolyte. For purpose of optimizing the performance of the supercapacitor, the ratio of positive and negative mass was matched according to formula S3 (Supporting information). According to the CV and GCD images in Fig. S10 (Supporting information), AC/CF presents a specific capacitance of 161.9 F/g at 1 A/g; m^- and m^+ refer to the mass of negative (15.5 mg) and positive electrodes (1 mg).

The voltage of supercapacitor is obtained from the CV curves of Ni-Co-S/$Co(OH)_2$ and AC electrodes (Fig. 4b). The voltage of two electrodes were −1∼0 V and 0∼0.6 V respectively, which proved that the operating voltage can reach to 1.6 V [54]. CV curves of the asymmetric supercapacitor with a potential voltage of 1.2∼1.7 V is shown in Fig. 4c; moreover, no significant change of the CV curves, indicating that the voltage to reach was feasible. CV shapes in Fig. 4d at 1.6 V are well maintained, indicating a favorable rate capability. The GCD curves at the voltage of 1.6 V of the asymmetric supercapacitor as shown Fig. 4e, the specific capacitances of the device are 164.4 F/g, 142.5 F/g, 131.3 F/g, 110.0 F/g, 100.0 F/g at 1 A/g, 2 A/g, 5 A/g, 8 A/g, 10 A/g, respectively. The rate curve of the device (Fig. 4f) showed that the specific capacitance can remain 60.8%

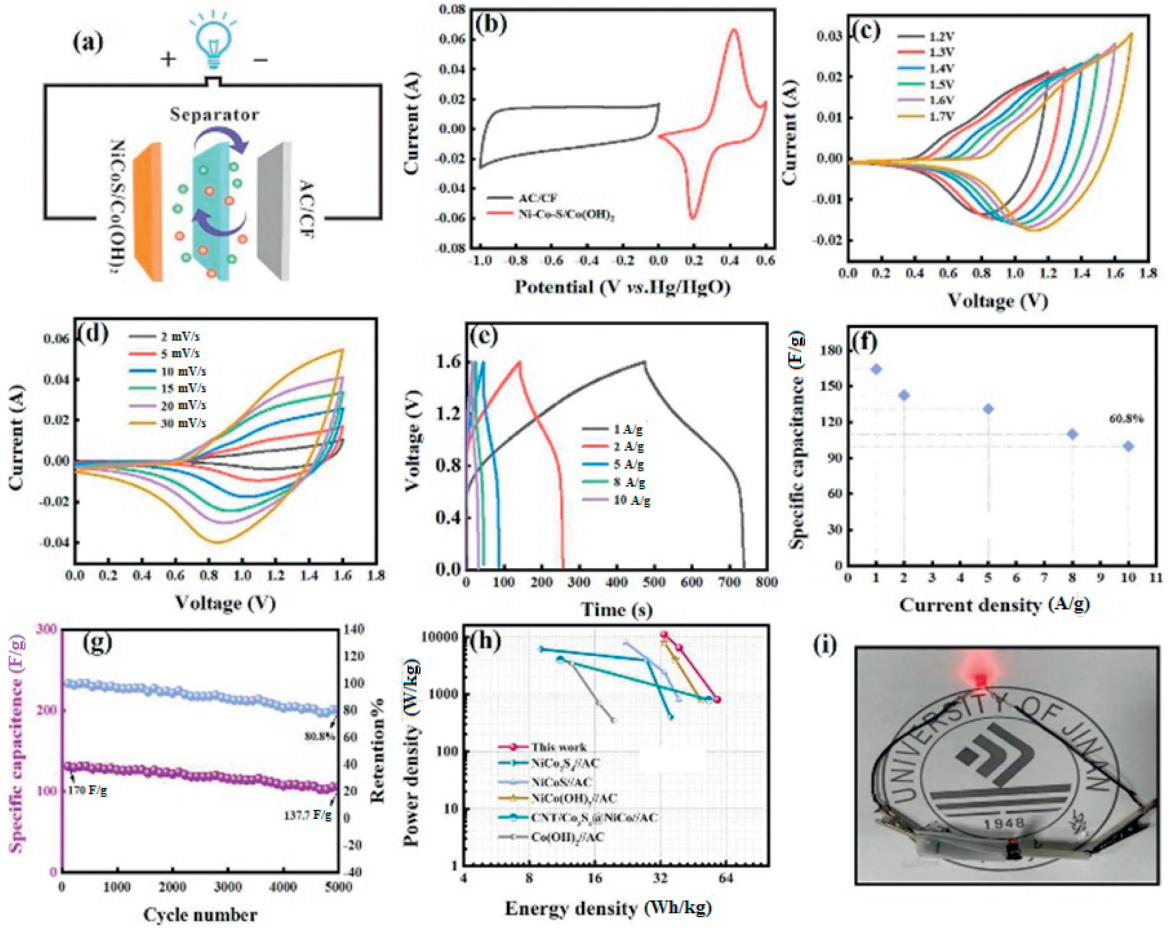

Fig. 4. (a) Schematic illustration of the Ni-Co-S/$Co(OH)_2$//AC hybrid supercapacitor. (b) CV curves of the Ni-Co-S/$Co(OH)_2$ and AC at 10 mV/s. (c) CV curves of the Ni-Co-S/$Co(OH)_2$//AC hybrid supercapacitor at 10 mV/s ranging from 0∼1.2 V to 0∼1.7 V. (d) CV curves of the Ni-Co-S/$Co(OH)_2$//AC hybrid supercapacitor with different scan rates in the voltage window of 0-1.6 V. (e) GCD curves of the as-assembled hybrid supercapacitor at different current densities. (f) The corresponding specific capacitances at different current densities. (g) Cycling performance of the assembled supercapacitor at a constant current density of 10 A/g. (h) Ragone plot of the as-assembled supercapacitor. (i) Light up an LED.

compared with the initial value at the high current density of 10 A/g. To detect the stability of the device, we carried out a cyclic test (Fig. 4g). After 5000 cycles, the specific capacitance remains 80.1% (137.7 F/g) compared with the initial value of 170 F/g. Furthermore, compared with recent reports (Fig. 4h), the asymmetric supercapacitors of Ni-Co-S/$Co(OH)_2$//AC excellent electrochemical performance (0.8 kW/kg at 210.4 Wh/kg), such as $NiCo_2S_4$//AC (0.8 kW/kg at 210.4 Wh/kg), NiCoS//AC (0.4 kW/kg at 128 Wh/kg), $NiCo(OH)_2$//AC (0.8 kW/kg at 140 Wh/kg), CNT/Co_3S_4 (0.8 kW/kg at 176 Wh/kg), NiCo LDH//AC (0.8 kW/kg at 192 Wh/kg), $Co(OH)_2$//AC (0.35 kW/kg at 69.9 Wh/kg) [55–62]. Fig. 4i displays the practical application of single asymmetric supercapacitor, exhibiting promising application potential.

In conclusion, the hollow structure of Ni-Co-S/$Co(OH)_2$ electrodes have been synthesized by multistep ion exchange, which yields excellent electrochemical performance, with ultra-high specific capacity (1440.0 C/g at 1 A/g), superior capacitance retention rate (79.1% retention at 20 A/g), and excellent cycling performance (81.4% retention after 5000 cycles). The corresponding supercapacitor has a high power density of 0.8 kW/kg when the energy density is 58.4 Wh/kg, and the capacitance was maintained at 80.8% compared with the initial capacitance. Our results will provide insights for the rational design of multicomponent transition metal sulfides and prominent electrodes for high-performance supercapacitors by manipulating cations and anions of metal compounds.

Declaration of competing interest

We declare that we do not have any commercial or associative interest that represents a conflict of interest in connection with the work submitted.

Acknowledgments

This work was supported by the National Natural Science Foundation of China (Nos. 51802177, 51672109) and the Independent Cultivation Program of Innovation Team of Ji'nan City (No. 2019GXRC011). All the authors discussed the results and commented on the manuscript.

Appendix A. Supplementary data

Supplementary material related to this article can be found, in the online version, at doi:https://doi.org/10.1016/j.cclet.2021.01.042.

References

[1] G.A. Snook, P. Kao, A.S. Best, J. Power Sources 196 (2011) 1–12.
[2] N. Choudhary, C. Li, J. Moore, et al., Adv. Mater. 29 (2017) 1605336.
[3] H. Luo, G.W. Wang, J.T. Lu, L. Zhuang, L. Xiao, ACS Appl. Mater. Inter. 11 (2019) 41215–41221.
[4] A. Borenstein, O. Hanna, R. Attias, et al., J. Mater. Chem. A 5 (2017) 12653–12672.
[5] M. Wang, Y.B. Tang, Adv. Energy Mater. 8 (2018) 1703320.
[6] W.D. He, C.G. Wang, H.Q. Li, et al., Adv. Energy Mater. 7 (2017) 1700983.
[7] J.Y. Cao, Y. Zhao, Y.F. Xu, et al., J Mater. Chem. A 6 (2018) 3355–3360.
[8] P.S. Kumar, P. Prakash, A. Srinivasan, C. Karuppiah, J. Power Sources 482 (2020) 228892.
[9] C.G. Wang, K. Guo, W.D. He, et al., Sci. Bull. 62 (2017) 1122–1131.
[10] J. Xie, Y.C. Lu, Nat. Commun. 11 (2020) 2499.
[11] Y. Merla, B. Wu, V. Yufit, et al., J. Power Sources 1 (2016) 224–231.
[12] G.J. He, M. Ling, X.Y. Han, et al., Energy Storage Mater. 9 (2017) 119–125.
[13] N. Feng, R.J. Meng, L.H. Zu, et al., Nat. Commun. 10 (2019) 1372.
[14] T.Z. Hao, Y.Y. Liu, G.L. Liu, et al., Energy Storage Mater. 23 (2019) 225–232.
[15] C.G. Wang, P.X. Sun, G.M. Qu, J.M. Yin, X.J. Xu, Chin. Chem. Lett. 29 (2018) 1731–1740.
[16] Y.F. Tang, Z.Y. Liu, W.F. Guo, et al., Electrochim. Acta 190 (2016) 118–125.
[17] Q. Rong, L.L. Long, X. Zhang, Y.X. Huang, H.Q. Yu, Appl. Energy 153 (2015) 63–69.
[18] M.H. Ye, L. Ma, M.Y. Gan, et al., Appl. Surf. Sci. 456 (2018) 390–397.
[19] N. Zhao, H.Q. Fan, M.C. Zhang, et al., Electrochim. Acta 321 (2019) 134681.
[20] G.M. Qu, C.L. Li, G. Zhao, et al., Nanoscale 7 (2020) 4686–4694.
[21] Y.X. Wen, S.L. Peng, Z.L. Wang, et al., J. Mater. Chem. A 15 (2017) 7144–7152.
[22] Q. Li, Y.X. Xu, S.S. Zheng, et al., Small 14 (2018) 1800426.
[23] Y. Li, F.F. An, H.R. Wu, et al., J. Power Sources 427 (2019) 138–144.
[24] R.S. Gao, Q.G. Zhang, F.Z. Soyekwo, et al., Electrochim. Acta 237 (2017) 94–101.
[25] S.H. Bi, Y.Z. Wu, A.Y. Cao, et al., Mater. Today Energy 1 (2020) 100548.
[26] Q.H. Wang, F. Gao, B.Y. Xu, et al., Chem. Eng. J. 327 (2017) 387–396.
[27] W.C. Jiang, D.S. Yu, Q. Zhang, et al., Energy Storage Mater. 25 (2015) 1063–1073.
[28] H.S. Han, H. Choi, S. Mhin, et al., Energy Environ. Sci. 8 (2019) 2443–2454.
[29] X.M. Yin, H.J. Li, H.Q. Wang, et al., ACS Appl. Mater. Inter. 10 (2018) 29496–29504.
[30] Q. Xue, H.B. Gan, Y. Huang, et al., Adv. Energy Mater. 8 (2018) 1703117.
[31] Y.Q. Xu, S.J. Hou, G. Yang, et al., Electrochim. Acta 285 (2018) 192–201.
[32] R.S. Gao, Q.G. Zhang, F. Soyekwo, et al., Electrochim. Acta 237 (2017) 94–101.
[33] J.X. Wang, C. Ma, Y.M. Choi, et al., J. Am. Chem. Soc. 34 (2011) 13551–13557.
[34] Y.Z. Su, K. Xiao, N. Li, Z.Q. Liu, S.Z. Qiao, J. Mater. Chem. A 34 (2014) 13845–13853.
[35] P.F. Cai, T. Liu, L.Y. Zhang, B. Cheng, J.G. Yu, Appl. Surf. Sci. 504 (2020) 144501.
[36] G.M. Qu, P.X. Sun, G.T. Xiang, et al., Appl. Mater. Today 20 (2020) 100713.
[37] G.M. Qu, X.X. Zhang, G.T. Xiang, et al., Chin. Chem. Lett. 31 (2020) 2007–2012.
[38] C.H. Liang, X.D. Zhang, P. Feng, H.X. Chai, Y.M. Huang, Chem. Eng. J. 344 (2018) 95–104.
[39] H.B. Wu, B.Y. Guan, P.L. He, X.Y. Yu, J. Mater. Chem. A 6 (2018) 19338–19341.
[40] X.H. Guan, M.H. Huang, L. Yang, G.S. Wang, X. Guan, Chem. Eng. J. 372 (2019) 151–162.
[41] W.R. Zou, W.X. Guo, X.Y. Liu, et al., Chem. Eng. J. 24 (2018) 19309–19316.
[42] T. Chen, Y.F. Tang, W.F. Guo, et al., Electrochim. Acta 212 (2018) 294–302.
[43] Y.Q. Jiang, J.P. Liu, Energy Environ. Mater. 2 (2019) 30–37.
[44] Y.R. Wei, X.X. ZHang, Z.H. Wang, et al., Chin. Chem. Lett. 32 (2021) 119–124.
[45] B.Y. Guan, X. Wang, S.Y. Song, X.W. Lou, Adv. Mater. 29 (2016) 1605051.
[46] J.F. Qian, F. Sun, L.Z. Qin, Mater. Lett. 82 (2012) 220–223.
[47] R. Li, S.L. Wang, Z.C. Huang, F.X. Lu, T.B. He, J. Power Sources 312 (2016) 156–164.
[48] Y.S. He, D.W. Bai, X.W. Yang, et al., Electrochem. Commun. 12 (2010) 570–573.
[49] H. Wang, C. Wang, C. Qing, et al., Electrochim. Acta 174 (2015) 1104–1112.
[50] Z.H. Wang, G.M. Qu, X.X. Zhang, et al., Nanoscale 35 (2020) 18400–18408.
[51] R. Li, S.L. Wang, Z.C. Huang, F.X. Lu, T.B. He, J. Power Sources 312 (2018) 156–164.
[52] S.D. Liu, Y. Yin, D.X. Ni, et al., Energy Storage Mater. 19 (2019) 186–196.
[53] X.L. Bai, X.L. Tong, Y.L. Gao, et al., Electrochim. Acta 281 (2018) 525–533.
[54] Z. Yu, Y. Bai, S.M. Zhang, et al., Int. J. Hydrogen Energy 43 (2018) 8815–8823.
[55] F.L. Zhao, W.X. Huang, D. Xie, et al., J. Mater. Sci. Mater. Electron. 20 (2019) 21229–21239.
[56] Y.X. Chen, C. Jing, X. Fu, et al., Chem. Eng. J. 384 (2020) 123367.
[57] W.S. Li, M.L. Chang, H.C. Cheng, Chem. Phys. Lett. 739 (2020) 137003.
[58] Y. Zhang, H. Liu, M. Huang, et al., ChemElectroChem 4 (2017) 721–727.
[59] Y.Y. Yang, P.L. Zhu, L.C. Zhang, et al., ACS Sustain. Chem. Eng. 7 (2019) 16803–16813.
[60] X.M. Wu, M. Lian, Q. Wang, Electrochim. Acta 295 (2019) 655–661.
[61] Q. Huang, J.Z. Wang, F. Lin, et al., RSC Adv. 20 (2016) 16745–16750.
[62] Y. Wang, W.C. Huo, X.Y. Yuan, Y.X. Zhang, Acta Phys. Chim. Sin. 36 (2020) 1904007.